npj computational materials

www.nature.com/npjcompumats

ARTICLE OPEN

Topological superconductor candidates $PdBi_2Te_4$ and $PdBi_2Te_5$ from a generic ab initio strategy

Aiyun Luo[1,5], Ying Li[1,5], Yi Qin[1,5], Jingnan Hu[1], Xiaoxu Wang[1], Jinyu Zou[1], Biao Lian[2] and Gang Xu[1,3,4]✉

Superconducting topological metals (SCTMs) have recently emerged as a promising platform of topological superconductivity (TSC) and Majorana zero modes for quantum computation. Despite their importance in both fundamental research and applications, SCTMs are very rare in nature. Here, we propose a strategy to design SCTMs by intercalating the superconducting units into the topological insulators. A program that characterizes the superconducting BdG Chern number of 2D BdG Hamiltonian from ab initio calculations is also developed. Following this strategy, $PdBi_2Te_5$ and $PdBi_2Te_4$ are found to be experimentally synthesizable and ideal SCTMs. Chiral TSC could be realized in such SCTMs by incorporating topological surface states with Zeeman effect, which can be realized by an external magnetic field or in proximity to ferromagnetic insulator. Our strategy provides a new method for identifying the SCTMs and TSC candidates, and the program makes it possible to design and modulate the TSC candidates from ab initio calculations.

npj Computational Materials (2023)9:188 ; https://doi.org/10.1038/s41524-023-01144-y

INTRODUCTION

As one of the most important systems in both fundamental physics and topological quantum computation, topological superconductors (TSCs) have attracted increasing interest for their ability to support Majorana fermions and anyons with non-Abelian statistics[1–18]. Currently, the search for TSCs candidates has been focused on two experimental schemes. One is the architecture by the combination of conventional superconductors with topological insulators[19–21] or 1D nanowires[22,23], but this approach brings high requirements for sample fabrication and interface engineering. The other route is to achieve TSCs in superconducting topological metals (SCTMs) that host both topological electronic structures at the Fermi level and superconductivity in one compound[24–40], in which the topological surface states are gapped by the "self-proximity effect" of bulk superconductivity, thus avoiding the complications of interface engineering. This approach has successfully predicted the SCTM $FeTe_{0.55}Se_{0.45}$[25–27] and similar compounds of iron-based superconductors[28–31], owing to the favorable superconducting gap and non-trivial band topology. Besides the Majorana zero modes, 1D helical/chiral Majorana states have also been reported in domain walls of $FeTe_{0.55}Se_{0.45}$[41] and the magnetism-superconductor heterostructures[42–49]. It is also proposed that the propagating chiral Majorana states can be applied to realize non-Abelian quantum gate operations, which could be 10^3 faster than the currently existing quantum computation schemes[50].

Encouraged by the success of Fe(Se, Te)[25–27], many topological materials that host both superconductivity and topological electronic structures are proposed[51–56]. However, very rare experimental progress of TSC has been made in such SCTMs. This is because, on the one hand, all of them are not the ideal SCTMs, whose band structures are too complicated, the topological surface states are usually buried in the bulk states, and difficult to form the pairing required by TSC. On the other hand, in addition to the prediction of some delicate 2D TSC systems from ab initio calculations[45,46], an extensional program that could calculate the TSC properties of SCTMs is not accessible.

In this work, we propose a new strategy to design ideal SCTMs by intercalating superconducting units into topological insulators. Following this strategy, $PdBi_2Te_5$ and $PdBi_2Te_4$ are ideal SCTMs that host topological surface states at the Fermi level and superconductivity at 0.57 K and 3.11 K respectively. To calculate the TSC properties of such SCTMs, we also develop a program to characterize the superconducting topological invariant of SCTM slab from ab initio calculations. By performing the superconducting energy spectrum and topological invariant calculations, we identify that chiral TSC could be realized in the slab of such SCTMs by introducing considerable Zeeman splitting on the topological surface states, which can be realized by an external magnetic field or in proximity to ferromagnetic insulators. Our strategy provides a new framework to enrich SCTMs and TSC candidates, and the program makes it possible to design and modulate the TSC system from ab initio calculations.

RESULTS

The calculation program

Inspired by the construction of magnetic topological insultor $MnBi_2Te_4$[57,58], we propose that the SCTMs can be designed by intercalating the superconductor units into the topological insulator, as illustrated by the schematic of Fig. 1a. As an ideal SCTM, the target crystal should be relatively stable in both energy and structure. More importantly, it must inherit the topological electronic structures of the parent topological insulator near the Fermi level, and also the superconductivity of the parent superconductor as shown in Fig. 1b. However, the combination of topological electronic structures and superconductivity does not result in TSC eventually. The realization of TSC generally requires a delicate modulation of many parameters, such as superconducting gap, Zeeman splitting and chemical potential, et al[19–27,42–49]. Thus, the ability to characterize the TSC

[1]Wuhan National High Magnetic Field Center & School of Physics, Huazhong University of Science and Technology, Wuhan, China. [2]Department of Physics, Princeton University, Princeton, NJ, USA. [3]Institute for Quantum Science and Engineering, Huazhong University of Science and Technology, Wuhan, China. [4]Wuhan Institute of Quantum Technology, Wuhan, China. [5]These authors contributed equally: Aiyun Luo, Ying Li, Yi Qin. ✉email: gangxu@hust.edu.cn

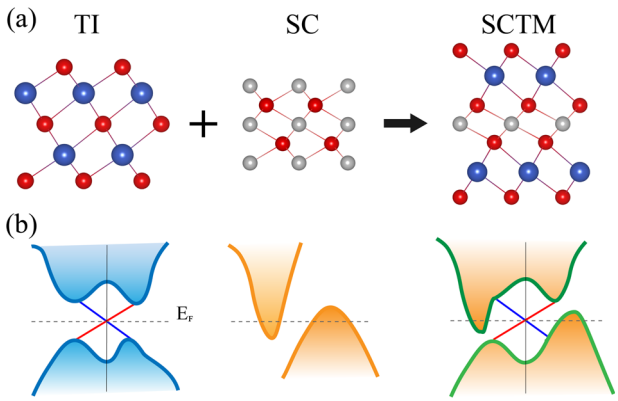

Fig. 1 The strategy to design idea superconducting topological metal (SCTM) by intercalating the superconductor (SC) units into the topological insulator (TI). a The illustration of the crystal structure. **b** The illustration of the band structure.

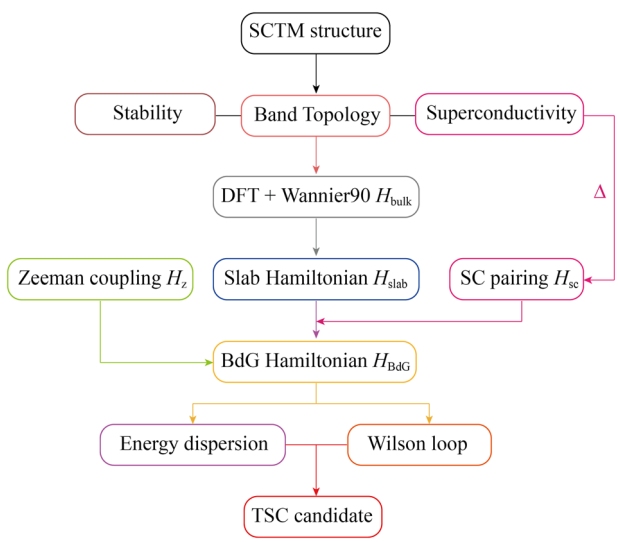

Fig. 2 The generic flow chart to characterize the TSC properties from ab initio calculations.

invariant and determine the required parameters in real materials from the ab initio calculations is not only of theoretical significance, but also highly desirable in experiment.

Here, parallel to previous studies on Class D TSC[45,46], we develop a program to simulate the supercondcuting properties and characterize its topological invariant in 2D slab system from ab initio calculations, in which the necessary ingredients to realize chiral TSC based on SCTM are included, such as bulk band structures, superconducting gap, Zeeman splitting, Rashba spin-orbit coupling and chemical potential. The workflow of this program is shown in Fig. 2. First, one should calculate the electronic structures of SCTM materials, and construct the localized Wannier functions that capture all electronic features from the first-principles calculations, referred as $\hat{H}_{\mathrm{bulk}}$. The next step is to construct the slab Hamiltonian $\hat{H}_{\mathrm{slab}}$ with open boundary condition along a certain direction[59]. In general, the spin-orbit coupling (SOC) and surface effect can be included automatically in $\hat{H}_{\mathrm{slab}}$ through the first-principles calculations with SOC. So that the topological properties, such as the surface states and spin-texture, can be directly studied by using $\hat{H}_{\mathrm{slab}}$. On the other hand, one can also construct a slab Hamiltonian $\hat{H}^{\mathrm{nsoc}}_{\mathrm{slab}}$ that excluded SOC from the non-SOC first-principles calculations, and add $\hat{H}_{\mathrm{SOC}}$ and $\hat{H}_{\mathrm{surf}}$ manually to simulate the variable SOC and surface effect in the topological electronic states and TSC, where the $\hat{H}_{\mathrm{surf}}$ would include surface potential difference, top/bottom surface hybridization etc.[44]. In this work, we will adopt the former type of $\hat{H}_{\mathrm{slab}}$, in which only the intrinsic SOC of the real material is included. With adopting particle-hole transformation, the $\hat{H}_{\mathrm{slab}}$ can be extended to BdG Hamiltonian $\hat{H}^{\mathrm{BdG}}_{\mathrm{slab}}$ by adding superconductor pairing $\hat{H}_{sc}$ and Zeeman splitting $\hat{H}_z$. In the Nambu basis $\Phi_{\mathbf{k}} = (c_{\mathbf{k},j,\alpha,\uparrow}, c_{\mathbf{k},j,\alpha,\downarrow}, c^{\dagger}_{-\mathbf{k},j,\alpha,\uparrow}, c^{\dagger}_{-\mathbf{k},j,\alpha,\downarrow})$, where the $c_{j,\alpha,\sigma}$ is the fermion operator denotes an electron at j layer with orbital α and spin $\sigma(\uparrow,\downarrow)$, the BdG Hamiltonian is formulated as:

$$H^{\mathrm{BdG}}_{\mathrm{slab}}(\mathbf{k}) = \begin{pmatrix} H_{\mathrm{slab}}(\mathbf{k}) - \mu & \Delta(\mathbf{k}) \\ \Delta^{\dagger}(\mathbf{k}) & -H^{*}_{\mathrm{slab}}(-\mathbf{k}) + \mu \end{pmatrix} + M_z\tau_z. \quad (1)$$

In Eq. (1), μ is the chemical potential, which can be used to simulate the carriers doping. $\Delta(\mathbf{k})$ denotes the superconductor pairing matrices, which could be both singlet and triplet pairing form. For the conventional s-wave superconductor, $\Delta(\mathbf{k})$ is expressed as:

$$\Delta(\mathbf{k}) = \Delta_s \times I_{slab} \otimes (i\sigma_y \otimes I_{orb}), \quad (2)$$

where Δ_s is the magnitude of intrinsic bulk s-wave pairing, σ_y is the Pauli matrix in spin space, I_{slab} (I_{orb}) is an $\mathcal{N}_{slab} \times \mathcal{N}_{slab}$ ($\mathcal{N}_{orb} \times \mathcal{N}_{orb}$) identity matrix that represents the number of slab layers (Wannier orbitals). τ_z is the Pauli matrix in particle-hole space, M_z is the Zeeman splitting energy, and $H_z = M_z\tau_z$ is used to simulate the influence of the external magnetic field or the proximity effect of the ferromagnetic insulator. Thus, H_z can be chosen to be applied for the whole slab or just few surface layers, depending on the slab thickness, strength of magnetic field, the type of superconductor etc. In principle, chiral TSC can be achieved by modulating the superconductor pairing, Zeeman splitting and chemical potential[42–49], which can be further revealed by calculating the superconducting energy spectrum and the superconducting topological invariant.

In the gapped 2D superconducting system, the topological superconductors are classified by BdG Chern number in the absence of time-reversal symmetry[3]. Such superconducting topological invariants can be characterized by the evolution of Wilson loop[60–62]. For the occupied quasiparticle states $\left|u^{\mathrm{BdG}}_{n,k_1,k_2}\right\rangle$, where k_1 and k_2 are momenta along two primitive vectors of the Brillouin zone, the Berry phase of the Wilson loop along k_2 at a fixed k_1 can be expressed as:

$$\mathcal{W}(k_1) = -\mathrm{Im}\ln\prod_i \det M_{k_1}{}^{(i)}, \quad (3)$$

with the overlap matrix $M^{(i)}_{k_1,mn} = \langle u^{\mathrm{BdG}}_{m,k_1,k_2^{(i)}} | u^{\mathrm{BdG}}_{n,k_1,k_2^{(i+1)}} \rangle$, where $k_2^{(i)}$ is the i-th discretized momenta along k_2 direction. The winding number of $\mathcal{W}(k_1)$ with respect to k_1 is equal to the superconducting BdG Chern number C_{BdG}.

The candidate materials

Next, we take topological insulator Bi_2Te_3[63,64], superconductor PdTe[65,66] and $PdTe_2$[54–56] as parent compounds to demonstrate that our SCTMs strategy is feasible. Experimentally, Bi_2Te_3 (space group $R\bar{3}m$, $a = 4.35$ Å, $c = 30.36$ Å), PdTe (space group space group $P6_3/mmc$, a = 4.152 Å, c = 5.671 Å, $T_c = 2.3$ K) and $PdTe_2$ (space group $P\bar{3}m1$, $a = 4.03$ Å, $c = 5.12$ Å, $T_c = 1.64$ K) all adopt the triangle lattice and have very similar in-plane lattice constants, which makes it much easier to integrate them together to form a new compound. According to our calculations, the stable unit of $PdBi_2Te_5$ and $PdBi_2Te_4$ adopt octuple-layer (OL) structure and septuple-layer (SL) structure respectively, as shown in Fig. 3a (also Supplementary Fig. 1)

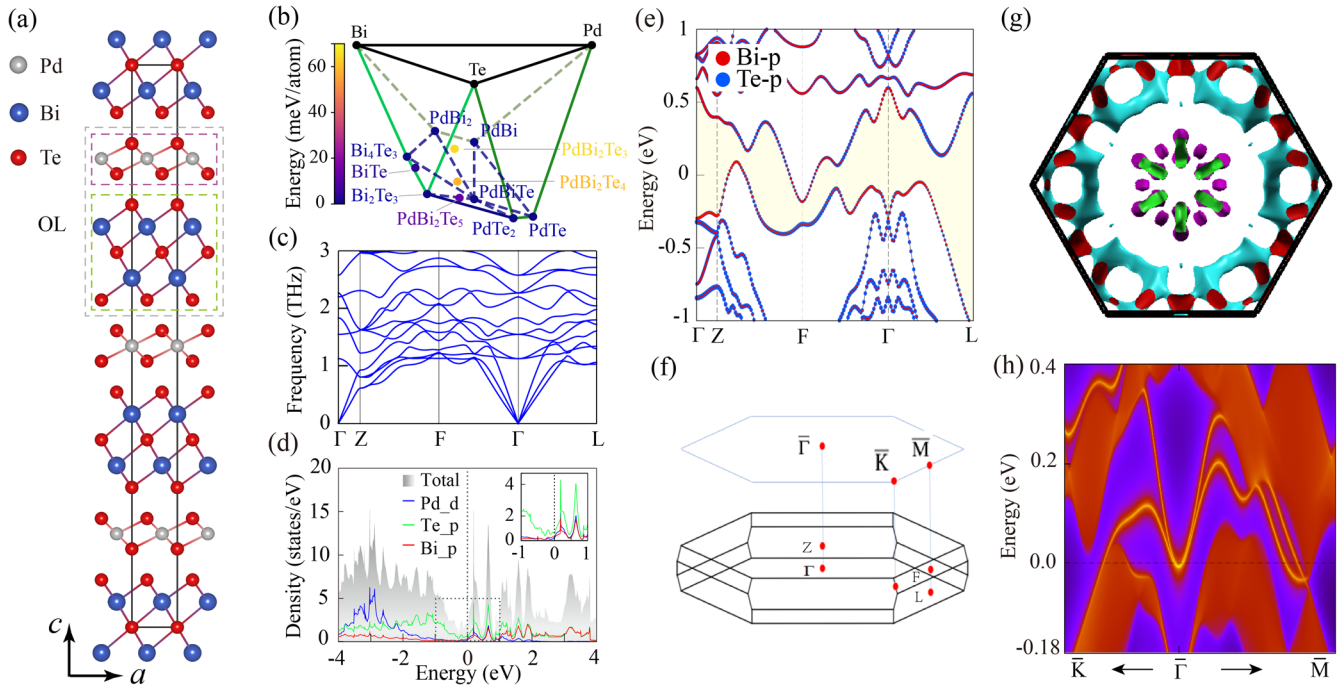

Fig. 3 The crystal and bans strucutre of $PdBi_2Te_5$. **a** The side view of the crystal structures of $PdBi_2Te_5$, in which the octuple-layer (OL) unit of $PdBi_2Te_5$ formed by the Bi_2Te_3 quintuple-layer and $PdTe_2$ triple-layer is marked by a gray dashed rectangle. **b** Convex hull diagram for Pd-Bi-Te system, the energy above convex hull is displayed by color-bar. **c** The phonon dispersion of $PdBi_2Te_5$. **d** The total DOS and projected DOS of the Pd, Te, Bi atoms in $PdBi_2Te_5$, the zoom-in image shows the projected DOS near the Fermi level. **e** The orbital-projected band structures of $PdBi_2Te_5$, where a continuous band gap around the Fermi level is marked by the yellow shade. **f** Brillouin zone and high-symmetry points. **g** The Fermi surfaces of bulk $PdBi_2Te_5$. **h** The topological surface states on (001) surface of $PdBi_2Te_5$.

and Supplementary Fig. 2 of Supplementary Material(SM)[67]. They both favor the ABC stacking along c-direction, and form the rhombohedral unit cell as shown in Fig. 3a, which is 73 meV/f.u. (73 meV/f.u. for $PdBi_2Te_4$) and 46 meV/f.u. (12 meV/f.u. $PdBi_2Te_4$) lower than the AA and AB stacking structures. The detailed crystal parameters and total energy of different stacking $PbBi_2Te_5$ and $PbBi_2Te_4$ are tabulated in the Supplementary Table 1 and Supplementary Table 2, respectively[67].

The formation energy of $PdBi_2Te_5$ and $PdBi_2Te_4$ are calculated to study their thermodynamic stability by using $E_f^{Pd_mBi_nTe_l} = E^{Pd_mBi_nTe_l} - mE^{Pd} - nE^{Bi} - lE^{Te}$, with E^i ($i = Pd_mBi_nTe_l$, Pd, Bi and Te) means the calculated total energy per formula in the ground state. The calculated $E_f^{PdBi_2Te_5}$ and $E_f^{PdBi_2Te_4}$ are − 3.184 eV/f.u. and − 2.476 eV/f.u., which means that 3.184 eV and 2.476 eV can be released during their synthesis processes from the constituent elements. To further manifest their thermodynamic stability, we construct the convex hull diagram in Fig. 3b with all of the synthesized Pd-Bi-Te compounds, whose crystal parameters and the calculated formation energy have been tabulated in Supplementary Table 3 and Supplementary Table 4, respectively[67]. Figure 3b shows that $PdBi_2Te_5$ and $PdBi_2Te_4$ are 13 meV/atom and 61 meV/atom above the convex hull respectively. Moreover, considering that metastable $PdBi_2Te_3$, 52 meV, and 3 meV higher than $PdBi_2Te_5$ and $PdBi_2Te_4$ as shown in Fig. 3b, has been synthesized in experiments[68,69], we thus conclude that $PdBi_2Te_5$ and $PdBi_2Te_4$ could be synthesized in experiments. For $PdBi_2Te_5$, we propose a synthetic route through the growth of Bi_2Te_3 and $PdTe_2$ layer by layer. Our calculated results reveal that bulk $PdBi_2Te_5$ is 59 meV/f.u. lower than the total energy of free standing Bi_2Te_3 and $PdTe_2$ layers, which strongly suggests that $PdTe_2$ layer tends to deposit on Bi_2Te_3 to form new $PdBi_2Te_5$ crystal. To investigate their dynamical stability, we calculate the phonon dispersion of $PdBi_2Te_5$ and $PdBi_2Te_4$, and plot them in Fig. 3c and Supplementary Fig. 3a[67]. There are 24 (21) phonon modes with fully real positive frequencies for $PdBi_2Te_5$ ($PdBi_2Te_4$), which indicates that the rhombohedral unit cells are dynamically stable. Based on these results, we conclude that $PdBi_2Te_5$ and $PdBi_2Te_4$ are relatively thermodynamically and dynamically stability in the rhombohedral structure, and further experimental investigation is called for.

Then we study the electronic structures and topological properties of $PdBi_2Te_5$ and $PdBi_2Te_4$. Since $PdBi_2Te_5$ and $PbBi_2Te_4$ exhibit similar electronic structures and non-trivial band topology, we only show the detailed density of states (DOS), band structures, and topological surface states of $PdBi_2Te_5$ as an example in the main text, one can check the results of $PdBi_2Te_4$ in Section III and Supplementary Fig. 3 of the SM[67]. In Fig. 3d, we plot the total and projected DOS of $PdBi_2Te_5$, which gives rise to DOS(0 eV) = 1.91 states/eV at Fermi level, indicating its metallic nature and the possibility of superconductivity. The projected DOS demonstrates that the states between −1 eV and 1 eV are dominated by the *p*-orbitals of Te hybridized with *d*-orbitals from Pd and *p*-orbitals from Bi. The hybridization is also manifested by the projected band structures shown in Fig. 3e, which shows that two bands with *p*-orbital components from Te or Bi cross the Fermi level and form several Fermi surfaces as demonstrated in Fig. 3g. Further detailed orbital components analysis demonstrates that a continuous band gap (yellow region in Fig. 3e) and band inversion exists between the nominal valence band and conduction band around the Fermi level, which implies that $PdBi_2Te_5$ inherits the topological electronic nature of Bi_2Te_3 successfully. The nontrivial band topology can be confirmed by calculating the Z_2 topological invariant of time-reversal invariant insulators[70]. Given that rhombohedral $PdBi_2Te_5$ possesses inversion symmetry and a continuous band gap, the Z_2 topological invariant $\nu_{TI} = (1 - P)/2$ is determined by the product P of the parity of the wave function at the points Γ, F, L, Z in Brillouin zone

(Fig. 3f)[70]. Our calculated results give Z_2 index $\nu_{TI} = 1$, confirming $PdBi_2Te_5$ is a Z_2 topological metal. To visualize the bulk-boundary correspondence, we calculate and plot the topological surface states on the (001) surface in Fig. 3h. The surface states are similar to that of Bi_2Te_3[63,64], the Dirac cone at the Γ point manifest approximately −6.3 meV below the Fermi level (the dashed line in Fig. 3h).

To investigate the superconducting property of $PdBi_2Te_5$, we perform the electron–phonon calculations based on density functional perturbation theory[71]. The electron-phonon coupling constant is obtained by integrating the Eliashberg function $\lambda = 2\int_0^{\infty} \alpha^2F(\omega)/\omega d\omega$[72], which gives $\lambda = 0.43$ for $PdBi_2Te_5$. For the logarithmic average phonon frequency, we find $\omega_{\log} = 97\,cm^{-1}$ as tabulated in Table. S5[67]. Furthermore, the superconducting transition temperature (T_c) is estimated by using the reduced Allen-Dynes formula[73,74]:

$$T_c = \frac{\omega_{\log}}{1.20}\exp\left[-\frac{1.04(1+\lambda)}{\lambda - \mu^*(1+0.62\lambda)}\right], \quad (4)$$

where μ^* is the effective Coulomb potential. By adopting a typical $\mu^* = 0.1$, the T_c of $PdBi_2Te_5$ is estimated as 0.57 K. As comparison, the calculated λ and $\omega_{\log}$ in $PdTe_2$ is 0.52 and 112 cm^{-1}, respectively. Accordingly, the estimated T_c in $PdTe_2$ is 1.59 K, which agrees well with the experimental T_c of 1.64 K[54–56].We also perform the electron-phonon coupling calculations for PdTe and $PdBi_2Te_4$. The estimated $T_c = 2.55$ K and $T_c = 3.11$ K for PdTe and $PdBi_2Te_4$ are listed in Table. S5[67]. All these results clearly demonstrate that the superconducting property in parent superconductors are well inherited into the new SCTMs. This is because the bond length and bond angle of Te-Pd-Te are very similar in $PdBi_2Te_5$ ($PdBi_2Te_4$) and $PdTe_2$ (PdTe), and the electron-phonon coupling in them are expected to be similar too. Since $PdTe_2$ and PdTe are conventional superconductors[54,75,76], it is reasonable to expect s-wave pairing for bulk $PdBi_2Te_5$ and $PdBi_2Te_4$ is expected. Using the BCS theory $2\Delta/k_BT_c \simeq 3.53$, the superconducting gap for $PdTe_2$, PdTe, $PdBi_2Te_5$ and $PdBi_2Te_4$ are estimated to be 0.29 meV, 0.38 meV, 0.09 meV and 0.47 meV respectively.

We now study the TSC property of the $PdBi_2Te_5$ slab by introducing the superconductor pairing and magnetic proximity effect into the topological surface states. Usually, the magnetic proximity effect is mainly dominated by the exchange coupling originated from the ferromagnetic substrate, resulting in spontaneous Zeeman splitting in the spin channel[49,77,78]. Hence, we only consider the Zeeman splitting in this work, as illustrated in Fig. 4a. As a concrete example, we use a 2D slab consisting of 10-OL $PdBi_2Te_5$, which is thick enough to avoid the hybridization between top layer and bottom layer (Fig. 3h). Since bulk $PdBi_2Te_5$ is expected as an intrinsic superconductor, the estimated s-wave pairing gap $\Delta = 0.09$ meV is introduced globally for all 10-OLs $PdBi_2Te_5$. As magnetic exchange coupling distance is about 1 nm[49,77,78] and the thickness of one surface layer is about 1.55 nm for $PdBi_2Te_5$, the out-of-plane Zeeman splitting is applied only in the bottom layer consisting of one $PdBi_2Te_5$ unit. The chemical potential μ is set at the energy of surface Dirac cone at the Γ point (about − 6.3 meV below the Fermi level). In Fig. 4b, we show the low energy spectrum of H_{BdG} at Γ point as a function of Zeeman splitting energy M_z, which manifest that the superconducting spectrum is fully gapped with an energy gap of Δ at $M_z = 0$. As M_z increases, the superconducting gap at the Γ point closes and reopens. This behavior indicates that a topological phase transition happens at critical point $M_z/\Delta = 3.1$, and this 2D slab enters chiral TSC phase characterized by a nonzero BdG Chern number and chiral Majorana edge states according to previous model simulations[42–44].

To firmly verify its topological property and visualize the low energy physics in the TSC phase, we calculate the superconducting energy spectrum at the condition $M_z = 5\Delta$ with the estimated $\Delta = 0.09$meV for bulk $PdBi_2Te_5$ in Fig. 4c. The corresponding Wilson loop evolutions for the occupied states are plotted in Fig. 4d. The zoom-in image of Fig. 4c reveals that a full superconducting gap is opened in the whole BZ, indicating that the system is a well defined chiral TSC. The Wilson loop evolution exhibits a nontrivial chiral winding number 1, which directly confirms the superconducting BdG Chern number $C_{BdG} = 1$. Given that the experimental accessible magnetization energy usually reaches a few MeV to tens of MeV, our results provide a feasible guideline for discovery the chiral TSC phase in $PdBi_2Te_5$.

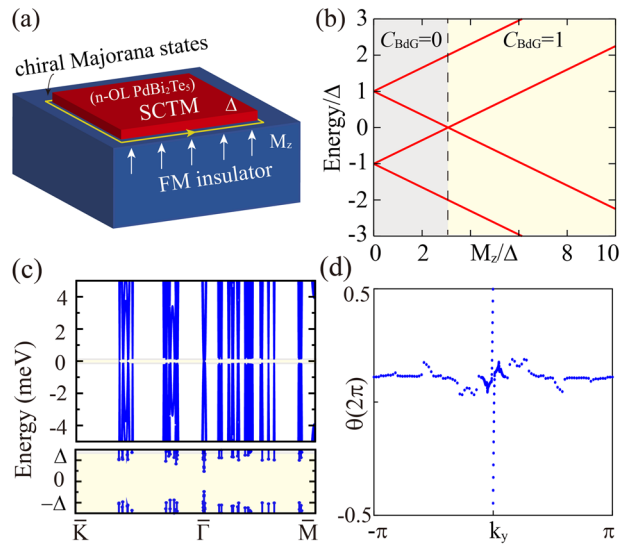

Fig. 4 The chiral TSC in $PdBi_2T_5$ slab. a The schematic to realize chiral TSC in $PdBi_2T_5$ slab. **b** The low energy spectrum at the Γ point as the function of Zeeman splitting energy M_z. **c** The superconducting spectrum along high symmetry paths with $M_z = 5\Delta$ and $\Delta = 0.09$ meV, the zoom-in image shows the full gap in the whole BZ. **d** The Wilson loop spectrum for all occupied states of **c**, which manifest the superconducting BdG Chern number $C_{BdG} = 1$ clearly.

DISCUSSION

Finally, we would like to point out that the chiral TSC phase could also be realized in $PdBi_2Te_4$ as shown in Supplementary Fig. 4[67], which exhibits a similar superconducting spectrum gap closing behavior with respect to M_z/Δ as in $PdBi_2Te_5$. In addition, we emphasize that our material design strategy can also be applied to search for other SCTM candidates. For example, our calculated results demonstrate that $AuBi_2Te_5$ formed by superconductor $AuTe_2$ interacting into Bi_2Te_3 is also an ideal SCTM, whose detailed crystal structures, dynamic stability, electronic structures, and topological surface states are discussed in Section V and Supplementary Fig. 5 of SM[67]. Therefore, we expect that SCTM $AuBi_2Te_5$ could also be a TSC candidate. Last, we would like to point out that the program can be extended to study many 2D topological superconducting heterostructure systems, such as magnetic topological insulator/superconductor heterostructure, ferromagnetic insulator/superconductor heterostructure and superconductor/topological insulator/superconductor heterostructure. This will make it possible to determine the accurate parameters of the TSC phase and simulate their TSC property in such systems from first-principles calculations. We expect our program to be also useful for optimizing the experimental setup, stimulating the field of TSC study.

METHODS

Calculation methods for the electron-phonon coupling constant

The first-principles calculations based on density functional theory are performed by the Vienna ab initio simulation package[79,80] with treating Perdew–Burke–Ernzerhof type of generalized gradient approximation as the exchange-correlation potential[81]. The cutoff energy for wave function expansion is set as 450 eV, k-points grid $13 \times 13 \times 13$ is used for sampling the first Brillouin zone. All crystal structures are fully optimized until the force on each atom is less than 0.01 eV/Å, and the SOC is included self-consistently. The electron-phonon coupling calculations with van der Waals correction[82] are carried out in Quantum Espresso[83] based on the perturbation theory. A Hermite-Gaussian smearing of 0.0025 Ryd is used for the electronic integration. The $8 \times 8 \times 8$ k-mesh is used for the electron–phonon coupling strength λ calculations, and the dynamical matrices are calculated on a $4 \times 4 \times 4$ phonon-momentum grid. Besides, a $2 \times 2 \times 2$ supercell is built to calculate the phonon dispersion by using PHONOPY[84]. Here, the electron-phonon coupling constant λ is calculated by integrating the Eliashberg function[72]:

$$\lambda = 2\int_0^{\infty} \alpha^2 F(\omega)/\omega d\omega, \tag{5}$$

where the electron-phonon interaction function $\alpha^2F(\omega)$ is calculated by summing contributions from each phonon branch:

$$\alpha^2 F(\omega) = \frac{1}{2\pi N(E_F)\sum_{\boldsymbol{q}\nu}} \delta\left(\omega - \omega_{\boldsymbol{q}\nu}\frac{\gamma_{\boldsymbol{q}\nu}}{\hbar\omega_{\boldsymbol{q}\nu}}\right), \tag{6}$$

where $\gamma_{\boldsymbol{q}\nu}$ is the phonon width, $\omega_{\boldsymbol{q}\nu}$ is the phonon frequency, and $N(E_F)$ is the electronic density states at the Fermi level. The $\gamma_{\boldsymbol{q}\nu}$ can be obtained self-consistently by density functional perturbation theory, giving by:

$$\gamma_{\boldsymbol{q}\nu} = \frac{2\pi\omega_{\boldsymbol{q}\nu}}{\Omega_{BZ}} \sum_{\boldsymbol{k},n,m} |g^{\nu}_{\boldsymbol{k},n;\boldsymbol{k}+\boldsymbol{q},m}|^2 \delta(\varepsilon_{\boldsymbol{k},n} - E_F)\delta(\varepsilon_{\boldsymbol{k}+\boldsymbol{q},m} - E_F), \tag{7}$$

where Ω_{BZ} is the volume of BZ, $\varepsilon_{\boldsymbol{k},n}$ and $\varepsilon_{\boldsymbol{k}+\boldsymbol{q},m}$ denote the Kohn-Sham energy, $g^{\nu}_{\boldsymbol{k},n;\boldsymbol{k}+\boldsymbol{q},m}$ denotes the electron-phonon coupling matrix.

The calculation methods for the surface

For the surface calculation, the Wannier functions of Pd-d, Bi-p and Te-p orbitals are constructed by using WANNIER90[85]. A slab consisting of 10-OL $PdBi_2Te_5$ layers with a bottom surface terminated as the Bi_2Te_3 layer is implemented in WannierTools[59], which is further used to calculate the electronic surface states, the superconducting spectrum, and the superconducting BdG Chern number.

DATA AVAILABILITY

All data are available upon reasonable request to the author.

CODE AVAILABILITY

All codes are available upon reasonable request to the author.

Received: 3 March 2023; Accepted: 29 September 2023;
Published online: 13 October 2023

REFERENCES

1. Nayak, C., Simon, S. H., Stern, A., Freedman, M. & Das Sarma, S. Non-abelian anyons and topological quantum computation. *Rev. Mod. Phys.* **80**, 1083–1159 (2008).
2. Sarma, S. D., Freedman, M. & Nayak, C. Majorana zero modes and topological quantum computation. *npj Quantum Inform.* **1**, 1–13 (2015).
3. Sato, M. & Ando, Y. Topological superconductors: a review. *Rep. Prog. Phys.* **80**, 076501 (2017).
4. Lutchyn, R. M. et al. Majorana zero modes in superconductor–semiconductor heterostructures. *Nat. Rev. Mater.* **3**, 52–68 (2018).
5. Liu, C.-X. & Trauzettel, B. Helical Dirac-Majorana interferometer in a superconductor/topological insulator sandwich structure. *Phys. Rev. B* **83**, 220510 (2011).
6. Zhang, F., Kane, C. L. & Mele, E. J. Time-reversal-invariant topological superconductivity and Majorana Kramers pairs. *Phys. Rev. Lett.* **111**, 056402 (2013).
7. Yang, S. A., Pan, H. & Zhang, F. Dirac and Weyl superconductors in three dimensions. *Phys. Rev. Lett.* **113**, 046401 (2014).
8. Wang, Q.-Z. & Liu, C.-X. Topological nonsymmorphic crystalline superconductors. *Phys. Rev. B* **93**, 020505 (2016).
9. Wang, Q., Liu, C.-C., Lu, Y.-M. & Zhang, F. High-temperature Majorana corner states. *Phys. Rev. Lett.* **121**, 186801 (2018).
10. Hao, N. & Hu, J. Topological quantum states of matter in iron-based superconductors: from concept to material realization. *Natl Sci. Rev.* **6**, 213–226 (2019).
11. Zhang, R.-X., Cole, W. S. & Das Sarma, S. Helical hinge Majorana modes in iron-based superconductors. *Phys. Rev. Lett.* **122**, 187001 (2019).
12. Zhang, R.-X., Cole, W. S., Wu, X. & Das Sarma, S. Higher-order topology and nodal topological superconductivity in Fe(Se,Te) heterostructures. *Phys. Rev. Lett.* **123**, 167001 (2019).
13. Zhang, R.-X. & Das Sarma, S. Intrinsic time-reversal-invariant topological superconductivity in thin films of iron-based superconductors. *Phys. Rev. Lett.* **126**, 137001 (2021).
14. Wu, X. et al. Boundary-obstructed topological high-T_c superconductivity in iron pnictides. *Phys. Rev. X* **10**, 041014 (2020).
15. Giwa, R. & Hosur, P. Fermi arc criterion for surface Majorana modes in superconducting time-reversal symmetric Weyl semimetals. *Phys. Rev. Lett.* **127**, 187002 (2021).
16. Nayak, A. K. et al. Evidence of topological boundary modes with topological nodal-point superconductivity. *Nat. Phys.* **17**, 1413–1419 (2021).
17. Margalit, G., Yan, B., Franz, M. & Oreg, Y. Chiral Majorana modes via proximity to a twisted cuprate bilayer. *Phys. Rev. B* **106**, 205424 (2022).
18. Zhou, X. et al. Topological superconductivity based on antisymmetric Spin-Orbit coupling. *Nano Lett.* **22**, 900–9005 (2022).
19. Fu, L. & Kane, C. L. Superconducting proximity effect and Majorana fermions at the surface of a topological insulator. *Phys. Rev. Lett.* **100**, 096407 (2008).
20. Xu, J.-P. et al. Experimental detection of a Majorana mode in the core of a magnetic vortex inside a topological insulator-superconductor $Bi_2Te_3/NbSe_2$ heterostructure. *Phys. Rev. Lett.* **114**, 017001 (2015).
21. Sun, H.-H. et al. Majorana zero mode detected with spin selective Andreev reflection in the vortex of a topological superconductor. *Phys. Rev. Lett.* **116**, 257003 (2016).
22. Mourik, V. et al. Signatures of Majorana fermions in hybrid superconductor-semiconductor nanowire devices. *Science* **336**, 1003–1007 (2012).
23. Nadj-Perge, S. et al. Observation of Majorana fermions in ferromagnetic atomic chains on a superconductor. *Science* **346**, 602–607 (2014).
24. Hosur, P., Ghaemi, P., Mong, R. S. K. & Vishwanath, A. Majorana modes at the ends of superconductor vortices in doped topological insulators. *Phys. Rev. Lett.* **107**, 097001 (2011).
25. Xu, G., Lian, B., Tang, P., Qi, X.-L. & Zhang, S.-C. Topological superconductivity on the surface of Fe-based superconductors. *Phys. Rev. Lett.* **117**, 047001 (2016).
26. Zhang, P. et al. Observation of topological superconductivity on the surface of an iron-based superconductor. *Science* **360**, 182–186 (2018).
27. Wang, D. et al. Evidence for Majorana bound states in an iron-based superconductor. *Science* **362**, 333–335 (2018).
28. Liu, Q. et al. Robust and clean Majorana zero mode in the vortex core of high-temperature superconductor $(Li_{0.84}Fe_{0.16})OHFeSe$. *Phys. Rev. X* **8**, 041056 (2018).
29. Liu, W. et al. A new majorana platform in an Fe-As bilayer superconductor. *Nat. Commun.* **11**, 1–7 (2020).
30. Kong, L. et al. Majorana zero modes in impurity-assisted vortex of LiFeAs superconductor. *Nat. Commun.* **12**, 1–11 (2021).
31. Li, M. et al. Ordered and tunable Majorana-zero-mode lattice in naturally strained LiFeAs. *Nature* 1–6 (2022).
32. Yuan, Y. et al. Evidence of anisotropic Majorana bound states in 2M-WS_2. *Nat. Phys.* **15**, 1046–1051 (2019).
33. Fang, Y. et al. Discovery of superconductivity in 2M WS_2 with possible topological surface states. *Adv. Mater.* **31**, 1901942 (2019).
34. Li, Y. et al. Observation of topological superconductivity in a stoichiometric transition metal dichalcogenide 2M-WS_2. *Nat. Commun.* **12**, 1–7 (2021).
35. Lv, Y.-F. et al. Experimental signature of topological superconductivity and Majorana zero modes on β-Bi_2Pd thin films. *Sci. Bull.* **62**, 852–856 (2017).

36. Guan, J.-Y. et al. Experimental evidence of anomalously large superconducting gap on topological surface state of β-Bi_2Pd film. *Sci. Bull.* **64**, 1215–1221 (2019).
37. Li, Y., Xu, X., Lee, M.-H., Chu, M.-W. & Chien, C. Observation of half-quantum flux in the unconventional superconductor β-Bi_2Pd. *Science* **366**, 238–241 (2019).
38. Wang, Z. H. et al. Topological edge states in a high-temperature superconductor FeSe/$SrTiO_3$ (001) film. *Nat. Mater.* **5**, 438–442 (2016).
39. Jin, K. H. et al. Topological superconducting phase in high-T_c superconductor MgB_2 with Dirac-nodal-line fermions. *npj Comput. Mater.* **5**, 57 (2019).
40. Zhou, X. et al. Observation of topological surface states in the high-temperature superconductor MgB_2. *Phys. Rev. B* **100**, 184511 (2019).
41. Wang, Z. et al. Evidence for dispersing 1D Majorana channels in an iron-based superconductor. *Science* **367**, 104–108 (2020).
42. Qi, X.-L., Hughes, T. L. & Zhang, S.-C. Chiral topological superconductor from the quantum Hall state. *Phys. Rev. B* **82**, 184516 (2010).
43. Wang, J., Zhou, Q., Lian, B. & Zhang, S.-C. Chiral topological superconductor and half-integer conductance plateau from quantum anomalous Hall plateau transition. *Phys. Rev. B* **92**, 064520 (2015).
44. He, J. J., Liang, T., Tanaka, Y. & Nagaosa, N. Platform of chiral Majorana edge modes and its quantum transport phenomena. *Commun. Phys.* **2**, 1–7 (2019).
45. Zhang, X. & Liu, F. Prediction of Majorana edge states from magnetized topological surface states. *Phys. Rev. B* **103**, 024405 (2021).
46. Zhang, X. et al. Prediction of intrinsic topological superconductivity in Mn-doped GeTe monolayer from first-principles. *npj Computat. Mater.* **7**, 1–8 (2021).
47. Ménard, G. C. et al. Two-dimensional topological superconductivity in Pb/Co/Si(111). *Nat. Commun.* **8**, 1–7 (2017).
48. Palacio-Morales, A. et al. Atomic-scale interface engineering of Majorana edge modes in a 2D magnet-superconductor hybrid system. *Sci. Adv.* **5**, eaav6600 (2019).
49. Kezilebieke, S. et al. Topological superconductivity in a van der Waals heterostructure. *Nature* **588**, 424–428 (2020).
50. Lian, B., Sun, X.-Q., Vaezi, A., Qi, X.-L. & Zhang, S.-C. Topological quantum computation based on chiral Majorana fermions. *Proc. Natl Acad. Sci. USA* **115**, 10938–10942 (2018).
51. Huang, K. et al. Observation of topological Dirac fermions and surface states in superconducting $BaSn_3$. *Phys. Rev. B* **103**, 155148 (2021).
52. Chen, C. et al. Observation of topological electronic structure in quasi-1D superconductor $TaSe_3$. *Matter* **3**, 2055–2065 (2020).
53. Ortiz, B. R. et al. CsV_3Sb_5: A $\mathbb{Z}_2$ topological kagome metal with a superconducting ground state. *Phys. Rev. Lett.* **125**, 247002 (2020).
54. Leng, H., Paulsen, C., Huang, Y. K. & de Visser, A. Type-I superconductivity in the Dirac semimetal $PdTe_2$. *Phys. Rev. B* **96**, 220506 (2017).
55. Das, S. et al. Conventional superconductivity in the type-II Dirac semimetal $PdTe_2$. *Phys. Rev. B* **97**, 014523 (2018).
56. Kudo, K., Ishii, H. & Nohara, M. Composition-induced structural instability and strong-coupling superconductivity in $Au_{1-x}Pd_xTe_2$. *Phys. Rev. B* **93**, 140505 (2016).
57. Lee, D. S. et al. Crystal structure, properties and nanostructuring of a new layered chalcogenide semiconductor, Bi_2MnTe_4. *CrystEngComm* **15**, 5532–5538 (2013).
58. Zhang, D. et al. Topological axion states in the magnetic insulator $MnBi_2Te_4$ with the quantized magnetoelectric effect. *Phys. Rev. Lett.* **122**, 206401 (2019).
59. Wu, Q., Zhang, S., Song, H.-F., Troyer, M. & Soluyanov, A. A. Wanniertools: an open-source software package for novel topological materials. *Computer Phys. Commun.* **224**, 405–416 (2018).
60. Yu, R., Qi, X. L., Bernevig, A., Fang, Z. & Dai, X. Equivalent expression of $\mathbb{Z}_2$ topological invariant for band insulators using the non-abelian berry connection. *Phys. Rev. B* **84**, 075119 (2011).
61. Soluyanov, A. A. & Vanderbilt, D. Computing topological invariants without inversion symmetry. *Phys. Rev. B* **83**, 235401 (2011).
62. Gresch, D. et al. Z_2pack: Numerical implementation of hybrid wannier centers for identifying topological materials. *Phys. Rev. B* **95**, 075146 (2017).
63. Zhang, H. et al. Topological insulators in Bi_2Se_3, Bi_2Te_3 and Sb_2Te_3 with a single Dirac cone on the surface. *Nat. Phys.* **5**, 438–442 (2009).
64. Chen, Y. et al. Experimental realization of a three-dimensional topological insulator, Bi_2Te_3. *Science* **325**, 178–181 (2009).
65. Matthias, B. T. Superconducting compounds of nonsuperconducting elements. *Phys. Rev.* **90**, 487–487 (1953).
66. Karki, A. B., Browne, D. A., Stadler, S., Li, J. & Jin, R. PdTe: a strongly coupled superconductor. *J. Phys.: Condens. Matter* **24**, 055701 (2012).
67. *See Supplemental Materials for more details, which includes I. The crystal structures of* $PdBi_2Te_5$ and $PdBi_2Te_4$. *II. The detailed crystal parameters and formation energies of Pd-Bi-Te compounds for convex hull. III. The phonon spectrum, electronic structures and superconducting properties of* $PdBi_2Te_4$. *IV. The chiral TSC phase in* $PdBi_2Te_4$. *V. The electronic structures and topological properties of* $AuBi_2Te_5$.
68. Sharma, M., Sang, L., Rani, P., Wang, X. & Awana, V. Bulk superconductivity below 6 K in $PdBi_2Te_3$ topological single crystal. *J. Superconductivity Nov. Magn.* **33**, 1243–1247 (2020).
69. Wang, X. et al. Identify the nematic superconductivity of topological superconductor $Pd_xBi_2Te_3$ by angle-dependent upper critical field measurement. *J. Superconductivity Nov. Magn.* **34**, 3045–3052 (2021).
70. Fu, L., Kane, C. L. & Mele, E. J. Topological insulators in three dimensions. *Phys. Rev. Lett.* **98**, 106803 (2007).
71. Baroni, S., de Gironcoli, S., Dal Corso, A. & Giannozzi, P. Phonons and related crystal properties from density-functional perturbation theory. *Rev. Mod. Phys.* **73**, 515–562 (2001).
72. Eliashberg, G. M. Interactions between electrons and lattice vibrations in a superconductor. *Sov. Phys. JETP* **11**, 696–702 (1960).
73. McMillan, W. L. Transition temperature of strong-coupled superconductors. *Phys. Rev.* **167**, 331–344 (1968).
74. Allen, P. B. & Dynes, R. C. Transition temperature of strong-coupled superconductors reanalyzed. *Phys. Rev. B* **12**, 905–922 (1975).
75. Masuko, M. et al. Nonreciprocal charge transport in topological superconductor candidate Bi_2Te_3/$PdTe_2$ heterostructure. *npj Quantum Mater.* **7**, 104 (2022).
76. Tiwari, B. et al. PdTe: a 4.5 K type-II BCS superconductor. *Supercond. Sci. Technol.* **28**, 055008 (2015).
77. Tang, C. et al. Magnetic proximity effect in graphene/$CrBr_3$ van der Waals heterostructures. *Adv. Mater.* **32**, 1908498 (2020).
78. Zhang, D. et al. Layer-resolved magnetic proximity effect in van der Waals heterostructures. *Nat. Nanotechnol.* **15**, 187–191 (2020).
79. Kresse, G. & Hafner, J. Ab initio molecular dynamics for open-shell transition metals. *Phys. Rev. B* **48**, 13115 (1993).
80. Kresse, G. & Furthmüller, J. Efficiency of ab-initio total energy calculations for metals and semiconductors using a plane-wave basis set. *Comput. Mater. Sci.* **6**, 15–50 (1996).
81. Perdew, J. P., Burke, K. & Ernzerhof, M. Generalized gradient approximation made simple. *Phys. Rev. Lett.* **77**, 3865–3868 (1996).
82. Klimeš, Jcv, Bowler, D. R. & Michaelides, A. Van der waals density functionals applied to solids. *Phys. Rev. B* **83**, 195131 (2011).
83. Giannozzi, P. et al. Quantum espresso: a modular and open-source software project for quantum simulations of materials. *J. Phys. Condens. Matter* **21**, 395502 (2009).
84. Togo, A. & Tanaka, I. First principles phonon calculations in materials science. *Scr. Mater.* **108**, 1–5 (2015).
85. Mostofi, A. A. et al. wannier90: A tool for obtaining maximally-localised wannier functions. *Comput Phys. Commun.* **178**, 685–699 (2008).

ACKNOWLEDGEMENTS

This work is supported by the National Key Research and Development Program of China (2018YFA0307000), and the National Natural Science Foundation of China (11874022). B.L. is supported by the Alfred P. Sloan Foundation, the National Science Foundation through Princeton University's Materials Research Science and Engineering Center DMR-2011750, and the National Science Foundation under award DMR-2141966.

AUTHOR CONTRIBUTIONS

G.X. conceived and designed the project. A.L., Y.L., and Y.Q. contributed to the work equally. A.L., Y.L., Y.Q., J.H., and X.W. performed all the DFT calculations. G.X., B.L., J.Z., and A.L. did the theoretical analysis. All authors contributed to the manuscript writing.

COMPETING INTERESTS

The authors declare no competing interests.

ADDITIONAL INFORMATION

Supplementary information The online version contains supplementary material available at https://doi.org/10.1038/s41524-023-01144-y.

Correspondence and requests for materials should be addressed to Gang Xu.